

Supporting Information for

Impact of Hydration on Ion Transport in $\text{Li}_2\text{Sn}_2\text{S}_5 \cdot x \text{H}_2\text{O}$

Markus Joos, Christian Schneider, Andreas Münchinger, Igor Moudrakovski, Robert Usiskin, Joachim Maier, and Bettina Lotsch

Experimental

Sample Preparation

$\text{Li}_2\text{Sn}_2\text{S}_5$ was synthesized from SnS_2 (precursor synthesized by heating a stoichiometric amount of Sn (99.8%, *Acros*) and S_8 (99.998%, *Sigma Aldrich*) with a slight excess of sulfur to 680 °C (12 h, 2 K/min)) and Li_2S (99.9%, *Alfa Aesar*). A small amount of excess sulfur was added to the stoichiometric mixture to ensure a sulfur-rich atmosphere during the reaction. The mixture was manually ground and mixed in a mortar and pestle, pressed into pellets, and transferred into a glassy carbon crucible inside a quartz ampoule. The ampoule (17 mm diameter, 12 cm length) was flame sealed under low vacuum and annealed (650 °C, 48 h, 2 K/min). A shiny violet powder was obtained. During cooling, residual sulfur condensed at the cold end of the ampoule and was discarded.

Samples of $\text{Li}_2\text{Sn}_2\text{S}_5 \cdot x \text{H}_2\text{O}$ with specific values of x were prepared by sealing anhydrous $\text{Li}_2\text{Sn}_2\text{S}_5$ powder in a glass container next to (but not in contact with) the desired amount of deionized water. The system was then allowed to equilibrate at 25 or 50 °C for at least 1-2 days. An additional synthesis was performed in the second TGA system described below. Another preparation method employed saturated salt solutions for humidification. Samples were placed in a custom-built desiccator containing the solution, a small fan as well as a sensor (SHT35, *Sensirion AG*) to measure both humidity and temperature. The samples were kept in the humid atmosphere for sufficiently long time to ensure equilibration at the respective humidities.

Compacts of the anhydrous material were prepared by uniaxial pressing (5 mm diameter, 10-20 kN (5-10 kbar), 1-5 min, 25 °C). In one case a 5 mm square die was used. The resulting pellets had thicknesses in the range 0.5-7.3 mm and were about 87% dense as determined by mass and volume measurements. In order to further densify samples of $\text{Li}_2\text{Sn}_2\text{S}_5 \cdot x \text{H}_2\text{O}$ ($x = 0$) different heat treatments were conducted:

Pressed 300 °C:

Pellet pressed with 10 kN (5 kbar), heated to 300 °C with 5 K/min, dwelled for 0.3 h, cooled to room temperature with 5 K/min; relative density of 92.5%

Pressed 25 °C, sintered 400 °C:

Pellet pressed at 25 °C with 10 kN (5 kbar), heated to 400 °C with 1 K/min in a S_8 flux, dwelled for 72 h, heated to 520 °C with 1 K/min, dwelled for 3 h, cooled to room temperature with 5 K/min; relative density of 86.7%

Pressed 25 °C, sintered 700 °C:

Pellet pressed at 25 °C with 15 kN (7.5 kbar), heated to 700 °C with 2 K/min in a S_8 rich atmosphere, dwelled for 48 h, cooled to room temperature with 2 K/min (similar to synthesis conditions); relative density of 87.8%

The sintering was done under vacuum either in Al_2O_3 or glassy-C crucibles inside quartz ampoules.

Compacts of the hydrated material were similarly prepared by uniaxial pressing (5 or 12 mm diameter, 0.1-1 min, 25 °C, 1.0-2.9 mm thickness). The material became softer with increasing water content, so the pressing force was decreased to 7-10 kN (3.5-5 kbar) for $0 < x \lesssim 3.0$ and about 0.1-1 kN (0.05-0.1 kbar) for $x \gtrsim 4.0$. For samples with $x \gtrsim 4.0$, pressing forces above this range were avoided, since they seemed to squeeze water out of the material. The relative density of the resulting compacts was estimated to be at least 79% for $0 < x \lesssim 3.0$, at least 72% for $x \approx 4.0$, and at least 61% for $x \approx 8.0$.

Thermogravimetric Analysis (TGA)

The TGA set-up used for synthesis employed a balance (*Mettler AT20*) magnetically coupled (*Rubotherm*) to a quartz glass crucible containing the sample powder. The sample chamber (double-walled brass container) was connected to a transfer stage, which was directly attached to a humidifier (double-walled glass container). The sample chamber, humidifier and transfer stage were temperature controlled within an accuracy of ± 0.05 K. To ensure sufficient water feeding for the humidifier, it was connected with a 4 L storage vessel positioned higher than the water level of the humidifier. The storage vessel was connected to a wobble piston pump, which would dropwise feed enough water into the humidifier. Water spill-over was controlled by an installed overflow drain positioned at half height and attached with a bubbler to prevent the humidified gas of escaping through the overflow drain. N_2 was used as protective and carrier gas (< 10 ppm H_2O including trace leaks, 40 ml/min) and the humidified gas after passing the sample would escape through a heated (180 °C) capillary-exhaust at the top of the sample chamber. The recorded weight gain was corrected using a two-dimensional (T and $p_{\text{H}_2\text{O}}$) buoyancy correction parameterized for the empty crucible.

X-Ray Powder Diffraction (XRPD)

Powder samples were sealed under dry inert gas in a polycarbonate dome (*PANalytical*). From previous experiments it was confirmed that the sample holder provides sufficient protection from atmosphere for ~24 h. XRPD patterns were measured at room temperature (*PANalytical* Empyrean Series 2 diffractometer, Bragg-Brentano configuration, Cu-K α , PIXcel 3D detector). The data were analyzed using HighScore Plus 3.0e (*PANalytical*).

Pulsed-Field Gradient Nuclear Magnetic Resonance (PFG NMR)

The magnetization data were fit by the following equations:

$$M(G) = M(0) \cdot \exp(-\gamma_i^2 D_{xy}^*(i) \cdot I(G)) \int_0^1 \exp(-\zeta \chi^2) d\chi \quad (1)$$

$$I(G) = G^2 \delta^2 \left(A - \frac{\delta}{3} \right) \text{ for a rectangular gradient pulse} \quad (2)$$

$$\zeta = (D_{xy}^*(i) - D_z^*(i)) \gamma_i^2 \cdot I(G) \quad (3)$$

$$D_{\text{eff}}^*(i) = \frac{2}{3} D_{xy}^*(i) + \frac{1}{3} D_z^*(i) \quad (4)$$

In the above equations, $M(G)$ and $M(0)$ are the area of the Fourier transformed attenuating spin-echo signal of the measured and maximum value; γ_i is the gyromagnetic ratio of nucleus i ; G and δ are the gradient strength and length of the pulse; A is the diffusion time; $I(G)$ is a double integral which can be represented with negligible error by the approximation in Equation (2); χ is an integration variable; and $D_{xy}^*(i)$, $D_z^*(i)$, and $D_{\text{eff}}^*(i)$ are the tracer diffusivities of species i in the xy and z directions as well as the overall effective tracer diffusivity. The fits were performed using the *nlinfit* function in Matlab (*Mathworks*, Version R2017a). The resulting fit curves were visually satisfactory, with a reasonable goodness of fit (typically $\chi^2 < 1.5$) and relatively small confidence intervals. Alternative models for data fitting were also tested which we will briefly discuss here (also see Figure S6). The first one was based on free, isotropic (3D) diffusion of ions with one mobile species (Stejskal and Tanner equation; $M(G) = M(0) \cdot \exp(-\gamma_i^2 G^2 D_{\text{iso}}^*(i) \delta^2 (A - \delta/3))$).¹ This model yielded visually unsatisfactory fits with larger goodness of fit and confidence intervals and was consequently discarded. The second model described 3D diffusion with two mobile species. This model was often as good if not superior to the one from Ref. 2, however, this could be attributed to the extra fitting parameter, and given that this model lacked in physical meaning, it was judged to be unsuited. The last alternative model was the same as in Ref. 2 yet allowing for out-of-plane diffusion ($D_z^*(i) \neq 0$). Similar to the second model, due to the additional parameter the fitting was often superior, but again it repeatedly produced unphysical results, and was therefore also dismissed. In principle, the non-linearity of the attenuation signals obtained in this work could also be partly caused by geometric confinement of the diffusing species, e.g., due to grain boundaries. However, based on the high fit quality for the 2D model, the degree of attenuation and the layered crystal structure, we judge that confinement effects have only a small impact on the observed signal, as discussed in the main text.

The 2D model yielded values for both the in-plane diffusivity $D_{xy}^*(\text{Li}^+)$ and the out-of-plane diffusivity $D_z^*(\text{Li}^+)$. The latter was found to be far smaller than the former, and the variance in $D_z^*(\text{Li}^+)$ was of the same order of magnitude as $D_z^*(\text{Li}^+)$ itself. In light of this large variance, $D_z^*(\text{Li}^+)$ could not be precisely determined, but we conclude that $D_z^*(\text{Li}^+)$ is at least one order of magnitude smaller than $D_{xy}^*(\text{Li}^+)$ for all conditions and water contents. The effective Li^+ diffusivity of the entire polycrystalline sample, $D_{\text{eff}}^*(\text{Li}^+)$, was calculated from an average over all possible orientations, according to the relation $D_{\text{eff}}^*(\text{Li}^+) = 2/3 D_{xy}^*(\text{Li}^+) + 1/3 D_z^*(\text{Li}^+) \approx 2/3 D_{xy}^*(\text{Li}^+)$.²

Electrochemical Measurements

For impedance measurements, compacts with $x < 3.0$ were contacted on both sides by ~ 400 nm thick ruthenium electrodes (99.95%, *Lesker*) applied by DC sputtering (*Emitech K575X*, 100 mA current, either 4 or 2 min sputter time) in a glovebox. A mask was used to prevent metal deposition on the sides of each sample. During sputtering the samples were exposed to high vacuum for several minutes, and the temperature increased to ~ 50 °C as measured by an adjacent thermocouple. This process caused a slight amount of water loss, which was accounted for by weighing. Typically, x decreased by ~ 0.5 . For compacts with $x \gtrsim 4.0$, electrical contact was sufficient without adding metal electrodes, so the sputtering step was omitted. All measurement cells and chambers were leak-checked in advance using a helium leak detector (UL 200 dry, *Oerlikon Leybold Vacuum*).

Anhydrous compacts ($x = 0$) were installed next to a thermocouple in an enclosed quartz holder in a tube furnace. Samples were heated to various temperatures under flowing inert gas (Ar or N_2 , 100 ml/min), and after a 1 h dwell, impedance spectra were acquired. Typically, two spectra were acquired at each condition to confirm reproducibility. Additional measurements were acquired at -133 to 27 °C by installing a compact in a cryostat (*LH Fluke Appliance*, He cooling) under high vacuum.

Hydrated samples ($x > 0$) were installed in a Teflon-lined tube fitting (*Swagelok*) and contacted by two rods that sealed to the fitting using Teflon ferrules. This cell was installed in a quartz tube, and measurements were performed as described above, except with a 0.5 h dwell between steps. Additional measurements at -69 to 27 °C were acquired by immersing the quartz tube containing the *Swagelok* cell in a thermostat-controlled silicone oil bath (thermostat FP90, silicone oil Thermal HY, *Julabo*).

For comparison, another setup (TSC Battery closed, *rhd instruments*) was employed in which powder samples were contacted directly by steel electrodes under a constant pressure of 30 kPa in a Microcell HC cell stand (1 h equilibration time). The results from this setup are shown as Dataset 2 in Figure S11.

Inductively Coupled Plasma Optical Emission Spectroscopy (ICP-OES)

Samples for ICP-OES were prepared by solubilizing fine ground powder in HNO_3 (65%) for 25 min at 185 °C with a microwave-assisted digestion system (Discover-SP-D). ICP-OES was performed with a Vista Pro Spectrometer (*Varian/Agilent Technologies*) with an axial plasma, Echelle grating polychromator, and a CCD-detector system. Data evaluation was performed with the software ICP-Expert.

Scanning Electron Microscopy (SEM) and Single Crystal Diffraction (SXRD)

Prior to SEM imaging, samples were placed on carbon tape and coated with ~2-3 nm carbon (ACE600, *Leica*). Micrographs were then acquired by a Zeiss microscope (Merlin) using SE2 (Everhart-Thomley type) and/or in-lens detectors. The transfer steps were performed under high vacuum and inert gas, with no air exposure.

For single crystal measurements, a suitable, transparent crystal (~10 x 10 x 5 μm^3) was picked in grease (*Dow Corning*) under a microscope in a glovebox. The crystal was mounted using grease on a 0.3 mm capillary (*Hilgenberg*, glass no. 14), inserted in a 0.5 mm capillary, and sealed with a hot wire under argon. Diffraction data were then collected at room temperature (Bruker AXS diffractometer, graphite-monochromated Mo-K α , SMART-APEX-II detector) and analyzed (Bruker Suite software, precession module).³

Thermogravimetric Analysis (TGA)

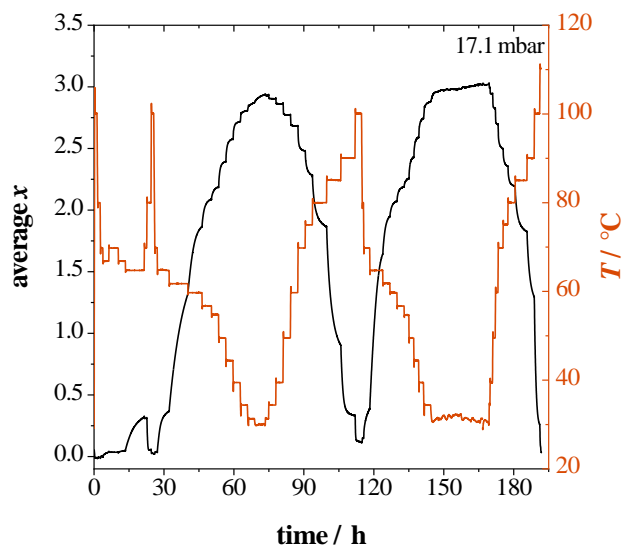


Figure S1: Typical TGA measurement of $\text{Li}_2\text{Sn}_2\text{S}_5 \cdot x \text{H}_2\text{O}$ at various temperatures and constant $p_{\text{H}_2\text{O}}$ of 17.1 mbar.

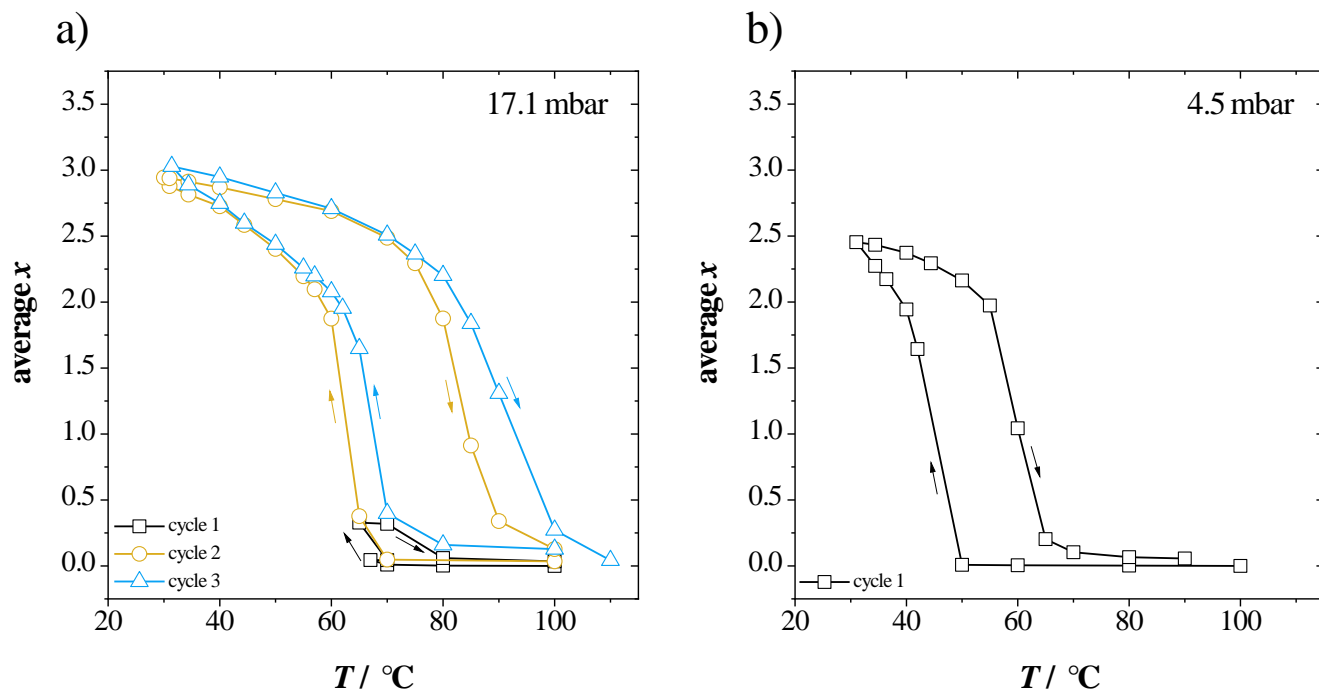


Figure S2: Degree of hydration x as a function of temperature T showing the hysteresis behavior of $\text{Li}_2\text{Sn}_2\text{S}_5 \cdot x \text{H}_2\text{O}$ at different isobaric conditions; (a) 17.1 mbar; (b) 4.5 mbar. For each measurement, freshly prepared anhydrous $\text{Li}_2\text{Sn}_2\text{S}_5$ was used as starting material.

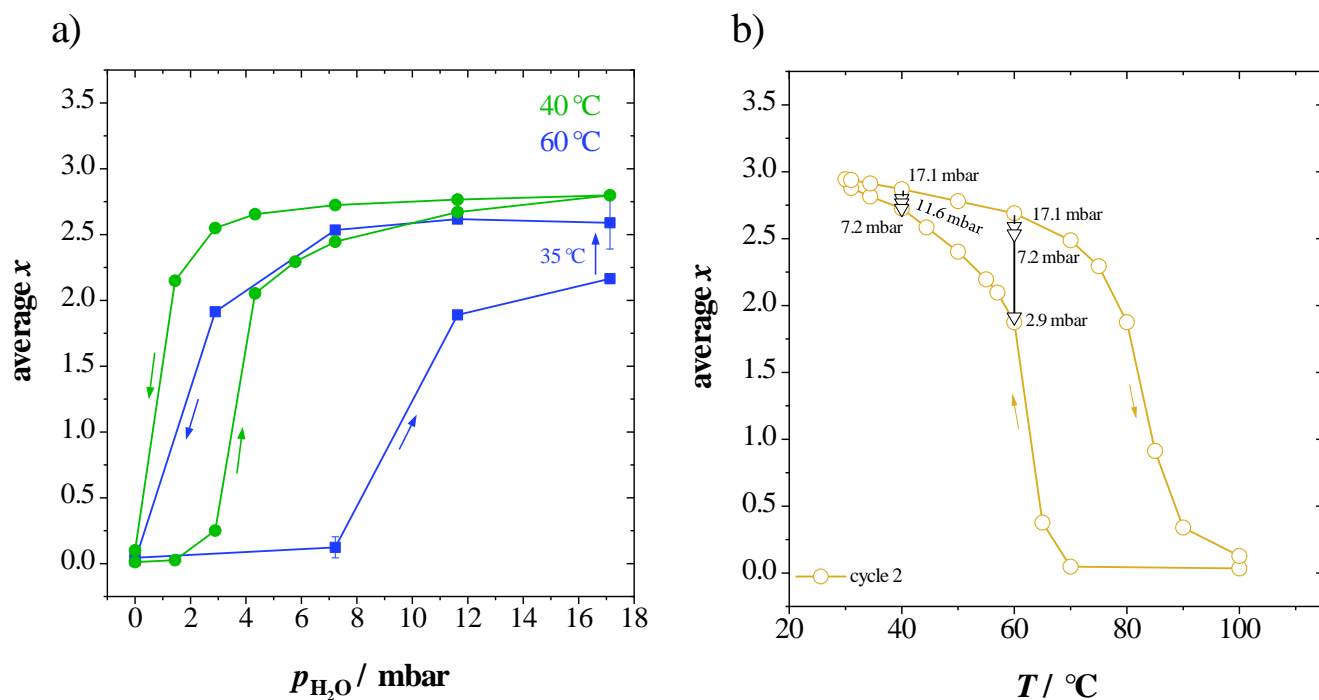


Figure S3: (a) Degree of hydration x as a function of partial pressure of water $p_{\text{H}_2\text{O}}$ showing the hysteresis behavior of $\text{Li}_2\text{Sn}_2\text{S}_5 \cdot x \text{H}_2\text{O}$ at the isothermal conditions for 40 $^{\circ}\text{C}$ and 60 $^{\circ}\text{C}$. For each measurement, freshly prepared anhydrous $\text{Li}_2\text{Sn}_2\text{S}_5$ was used as starting material.; (b) Isobaric measurement of $\text{Li}_2\text{Sn}_2\text{S}_5 \cdot x \text{H}_2\text{O}$ at 17.1 mbar shown in Figure S2a with inserted data points from the isothermal measurement.

The mass change during hydration was found to be initially proportional to time (Figure S4b).⁴ It is unclear if this dependence arises from bulk- or surface-limited behavior, since the water diffusivity strongly increases with increasing water content. We think the kinetics are probably bulk-limited, as discussed in the main text. However, if the kinetics are surface-limited, then the surface exchange constant \bar{k} can be estimated from the relation $\bar{k} = 0.5 \cdot (L_{1/2}/t_{1/2})$, where $L_{1/2}$ is the particle radius ($\sim 25 \mu\text{m}$) and $t_{1/2}$ is the time at which the mass uptake is halfway finished.⁴ For example, a value of $1.3 \times 10^{-7} \text{ cm/s}$ at $39 \text{ }^\circ\text{C}$ is obtained.

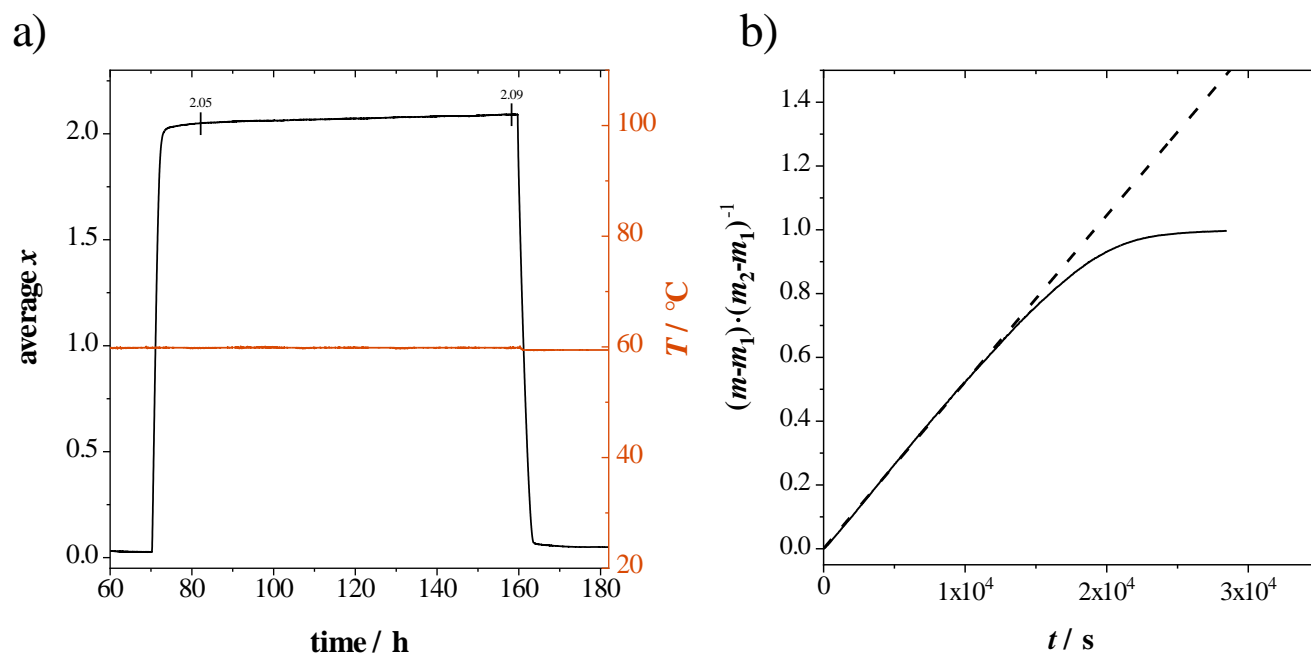


Figure S4: (a) Long-time TGA measurement of $\text{Li}_2\text{Sn}_2\text{S}_5 \cdot x \text{H}_2\text{O}$ at constant $p_{\text{H}_2\text{O}}$ (17.1 mbar) and temperature ($60 \text{ }^\circ\text{C}$); (b) Normalized mass change for the measurement in Figure 1a; here m , m_1 , and m_2 are the mass at time t , the initial mass, and the mass at equilibration.

Pulsed-Field Gradient Nuclear Magnetic Resonance (PFG NMR)

Figure S5 shows the effective diffusivity as a function of diffusion time for three values of the water content, as well as at different temperatures for $x \approx 8.0$. It is evident that the obtained value of $D_{\text{eff}}^*(\text{Li}^+)$ decreases slightly (by a factor of 1.5-3) when the diffusion time is increased from 10 to 100 ms. This behavior can be attributed to slightly slower transport at grain boundaries, as discussed previously.⁵ If so, then to be precise, the in-plane diffusivity within a single grain is best estimated by $D_{xy}^*(\text{Li}^+)$ measured at a shorter diffusion time, although the true value in the absence of all boundaries may be slightly higher. The effective diffusivity across a randomly oriented polycrystalline sample is best estimated by $D_{\text{eff}}^*(\text{Li}^+)$ measured at a longer diffusion time, although the true DC value when all boundaries are accounted for may be slightly lower.

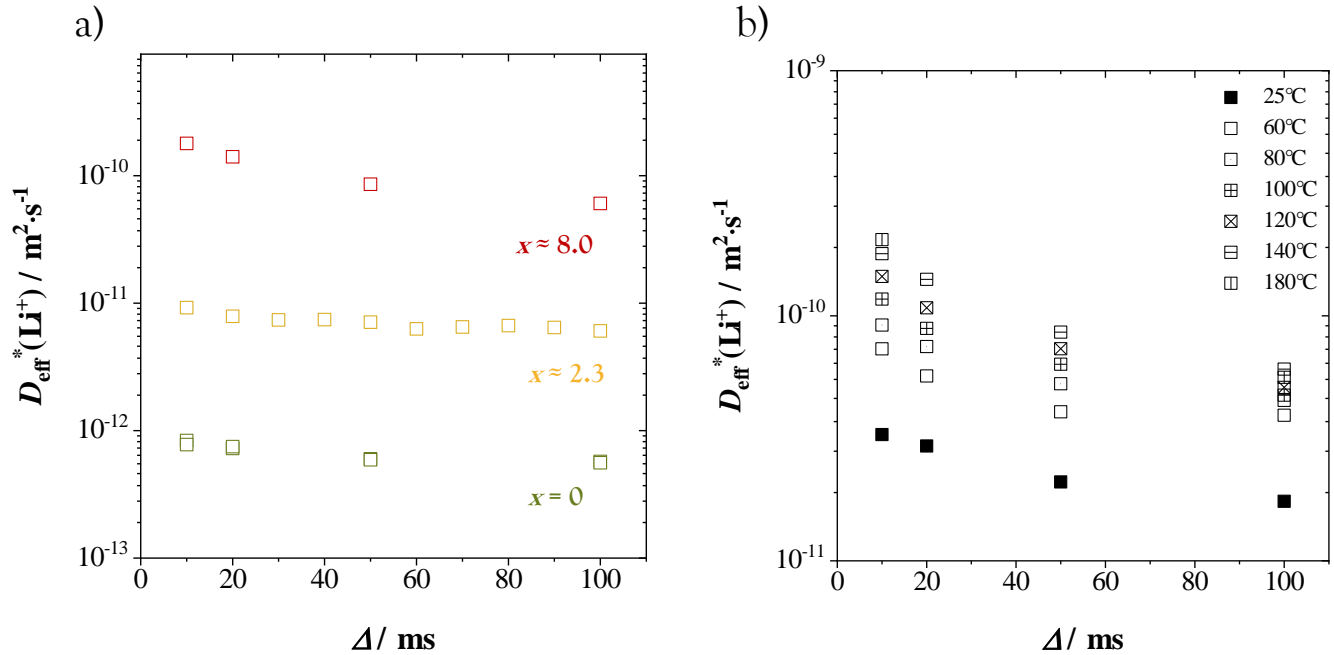


Figure S5: Effective Li^+ tracer diffusivity extracted from ^7Li PFG NMR measurements with various diffusion times using the 2D diffusion model: (a) $x = 0$ (140 °C), $x \approx 2.3$ (180 °C) and $x \approx 8.0$ (140 °C); (b) $x \approx 8.0$ at various temperatures.

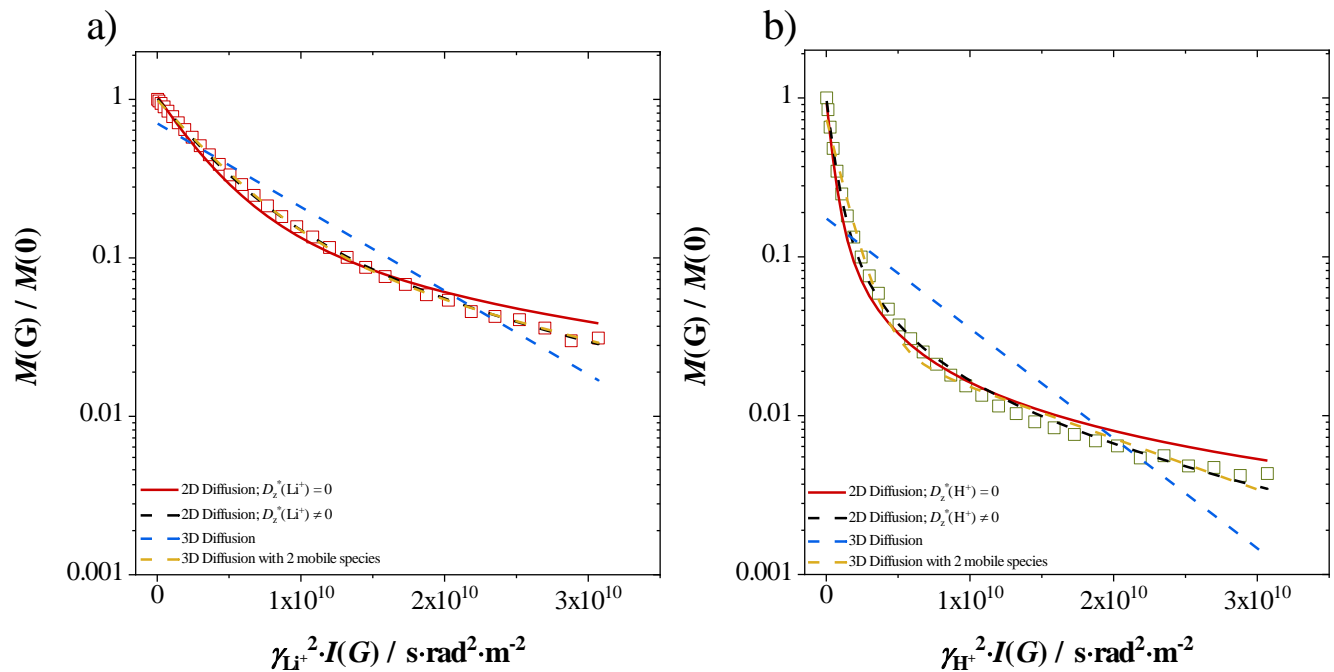


Figure S6: Comparison of PFG NMR fits in $\text{Li}_2\text{Sn}_2\text{S}_5 \cdot x \text{H}_2\text{O}$ ($x \approx 8.0$, 70 °C) using different diffusion models; (a) Li^+ diffusion, (b) H^+ diffusion.

Solid State Nuclear Magnetic Resonance (ssNMR)

Anhydrous $\text{Li}_2\text{Sn}_2\text{S}_5$ was measured by ssNMR to record both its relaxation time T_1 and the full width at half maximum (FWHM) of the peaks (Figure S7). Using the equation $(T_1)^{-1} = F \cdot (\tau_c^\circ)^{-1} \exp(-E_A^{\text{LT}}/(k_B T))$; where F is a constant, τ_c° is the correlation time of the Larmor frequency, E_A^{LT} is the activation energy at low temperatures and k_B is the Boltzmann constant;⁶ one can estimate E_A^{LT} from linearly fitting the low temperature branch, yielding 0.05 eV for anhydrous $\text{Li}_2\text{Sn}_2\text{S}_5$. This very low activation energy, however, does not correspond to the long-range migration enthalpy recorded by PFG NMR and impedance, and rather reflects a local hopping of ions. The recorded FWHM can be analyzed with the empirical expression $E_A = 1.617 \times 10^{-3} \cdot T_c / \text{K}$, where T_c is the onset temperature of motional narrowing.^{7,8} The resulting activation energy is 0.56 eV for high temperatures. Even though this value is not far from the ones measured by PFG NMR and impedance, one should keep in mind the empirical nature of this method.

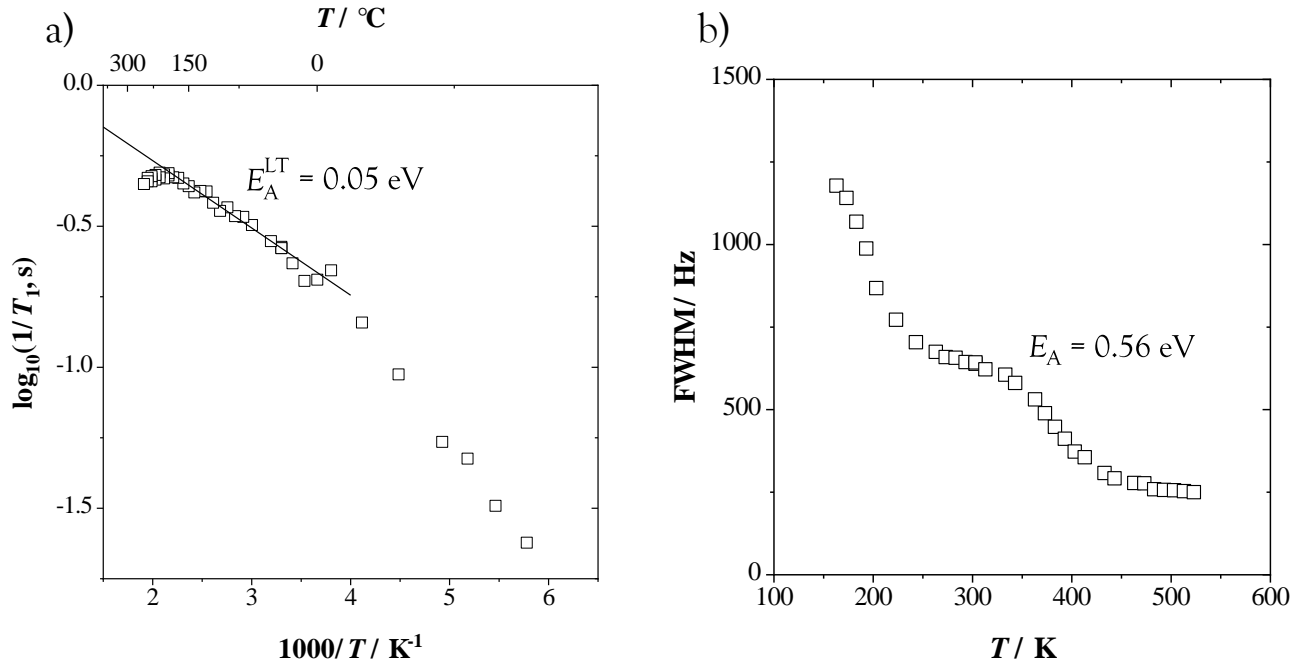


Figure S7: (a) NMR relaxometry measurement of $\text{Li}_2\text{Sn}_2\text{S}_5 \cdot x \text{H}_2\text{O}$ ($x = 0$) at different temperatures. The low temperature regime is fitted linearly to yield a low activation energy of $E_A^{\text{LT}} = 0.05 \text{ eV}$; (b) Plot showing the Full Width at Half Maximum (FWHM), also referred to as motional narrowing, of $\text{Li}_2\text{Sn}_2\text{S}_5 \cdot x \text{H}_2\text{O}$ ($x = 0$) at different temperatures. The onset temperature yields an activation energy of $E_A = 0.56 \text{ eV}$.⁸

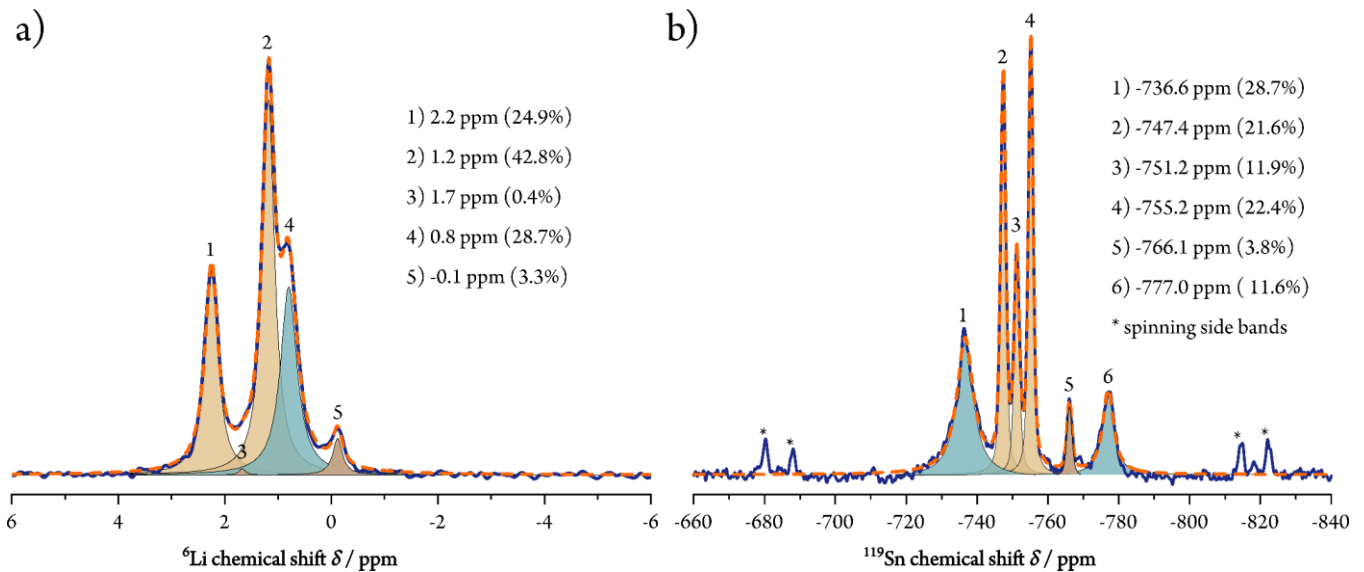


Figure S8: (a) ^6Li and (b) ^{119}Sn MAS NMR spectra of anhydrous $\text{Li}_2\text{Sn}_2\text{S}_5$ (single batch). Brown colored signals correspond to crystalline material, while turquoise colored signals are broader and are attributed to a disordered side phase and/or stacking faults. Signals 3 and 5 in the ^6Li and signal 5 in the ^{119}Sn spectrum are assigned to $\text{Li}_2\text{Sn}_2\text{S}_3$. Slight batch-to-batch variations were observed in the ^6Li spectra.

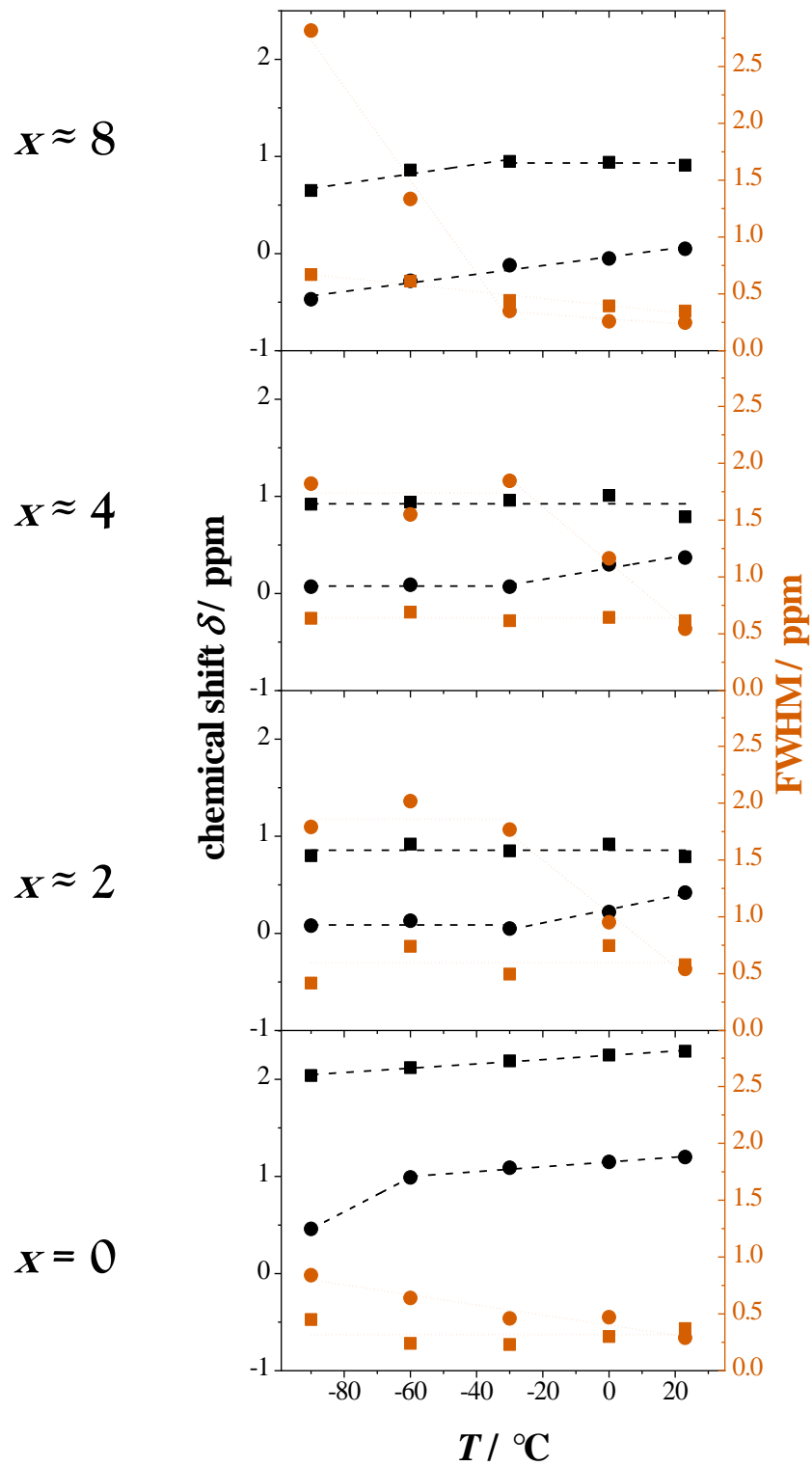


Figure S9: Chemical shifts δ (black) and full widths at half-maximum FWHM (red) for signal 1 (squares) and signal 2 (circles) in the ^6Li NMR spectra in Figure 5. Dashed and dotted lines are guides for the eye. Although motional narrowing is theoretically accompanied by a transition from a Gaussian to a Lorentzian line shape, for simplicity a Lorentzian line shape was used in all fits.

Electrochemical Measurements

To convert the by PFG NMR measured diffusivities into conductivity with the Nernst-Einstein relation (see equation (2) in the main text), the lithium ion concentration $[\text{Li}^+]$ was estimated with:

$$[\text{Li}^+] = \frac{d_0}{d_x} \cdot \frac{Z_{\text{Li}}}{V_{\text{UC}}} \quad (5)$$

where d_0 and d_x are the interlayer spacing for $x = 0$ and $x > 0$ (see Figure 2), Z_{Li} and V_{UC} are the number of Li atoms (3.78) and volume (438.8 \AA^3) per unit cell for $x = 0$. Note that the here estimated concentration is an upper bound, since, at least for $x = 0$, it is unclear how crystallinity affects the ionic transport (referring to the less crystalline content seen in Figure 5).

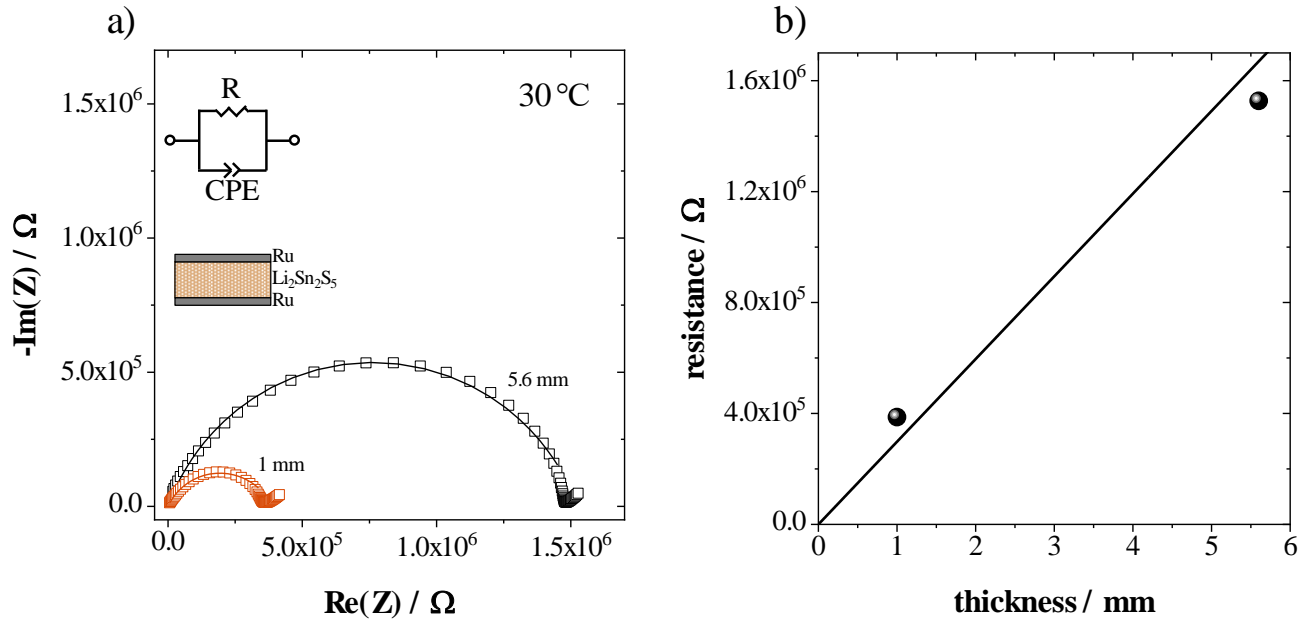


Figure S10: Impedance measurements of $\text{Li}_2\text{Sn}_2\text{S}_5 \cdot x \text{H}_2\text{O}$ ($x = 0$) with different sample thicknesses showing (a) the impedance spectra and (b) the linear scaling of the resistance with thickness. The line is a linear fit going through 0.

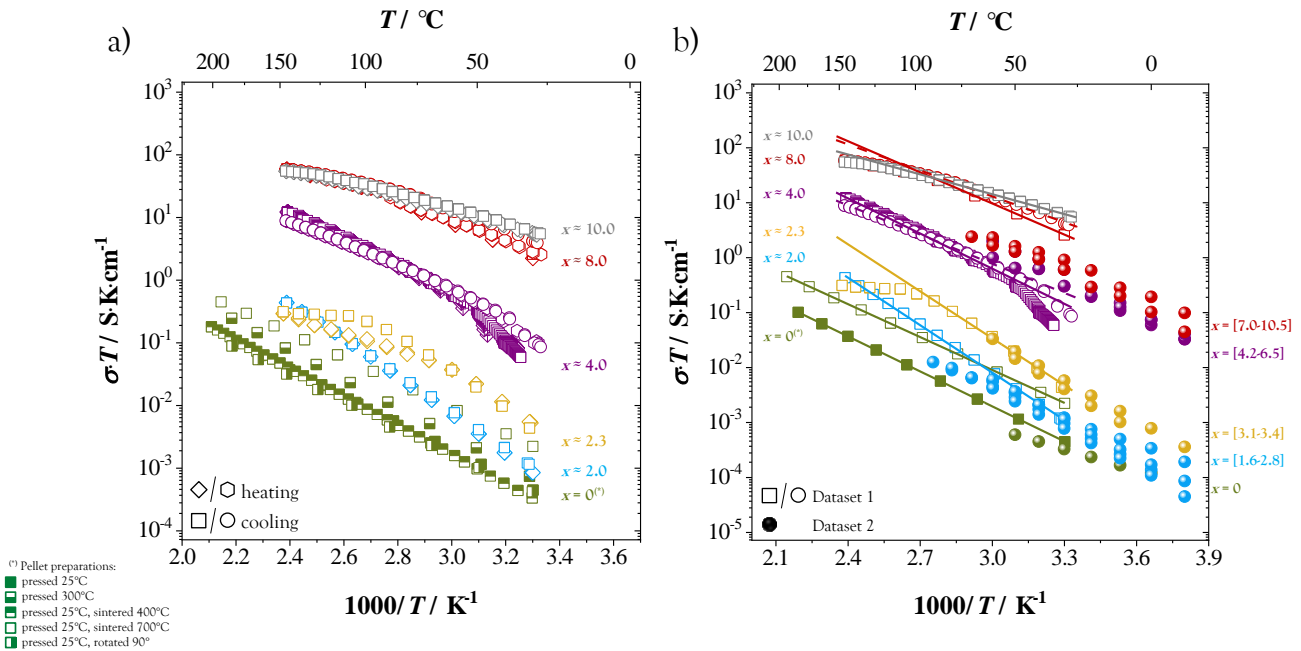


Figure S11: (a) Temperature dependence of the conductivity measured from $\text{Li}_2\text{Sn}_2\text{S}_5 \cdot x \text{H}_2\text{O}$ by impedance spectroscopy showing different sample preparation methods for $x = 0$ as well as heating and cooling runs for $x > 0$. (b) Comparison of impedance data of $\text{Li}_2\text{Sn}_2\text{S}_5 \cdot x \text{H}_2\text{O}$ collected at two different experimental set-ups. Solid lines are linear fits.

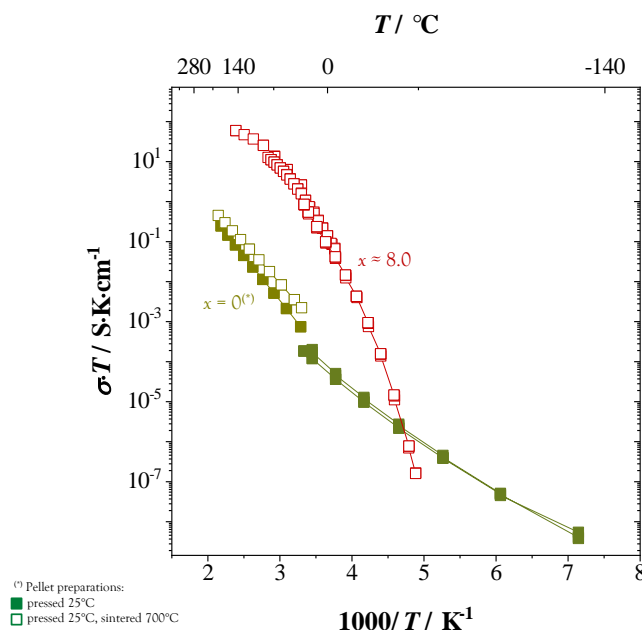


Figure S12: Transport data for $\text{Li}_2\text{Sn}_2\text{S}_5 \cdot x \text{H}_2\text{O}$ ($x = 0$ and $x \approx 8.0$) measured above and below room temperature. For $x = 0$, two datasets are shown: pellet pressed at 25°C (closed squares); pellet pressed at 25°C, sintered at 700°C (open squares).

Electromotive force (EMF) and conductivity measurements were performed with Li^+ reversible electrodes, for which anhydrous compacts were sandwiched between Li (99.9%, *Alfa Aesar*) and LiAl (> 99.5%, *ELSAindustries SAS*) electrodes (Figure S13). LiAl powder was co-pressed with $\text{Li}_2\text{Sn}_2\text{S}_5$ powder, while slabs of Li were applied directly to the compacts. The Li^+ reversible electrodes themselves were contacted by either stainless steel rods or disks of molybdenum to avoid alloying of the metals. The measurement conditions were the same as described for the Li^+ blocking electrodes in the main text. The measured EMF was 0.32 V initially, close to the Nernst voltage expected for these electrodes.⁹ Over tens of hours it decreased to below 0.05 V, while the conductivity increased gradually to $\sim 10^{-4}$ S/cm and the dielectric constant ϵ_r increased from ~ 100 to ~ 4000 . If instead noble metal electrodes are used, DC polarization experiments indicate pure ionic conduction,⁵ as does the blocking impedance arc at low frequencies observed in this study. Taken together, these observations indicate that $\text{Li}_2\text{Sn}_2\text{S}_5$ is a predominant ion conductor, which however reacts in contact with Li alloy electrodes to yield a phase with substantial electronic conductivity.

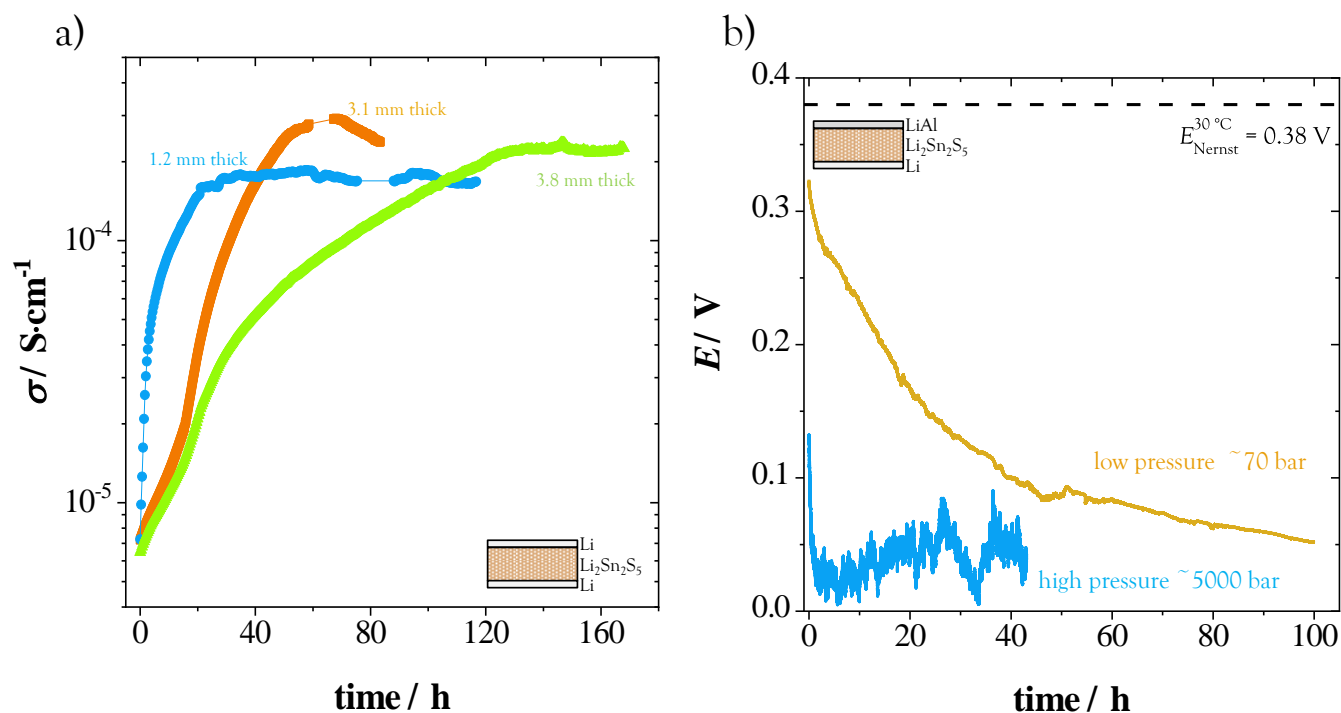


Figure S13: (a) Conductivity of anhydrous $\text{Li}_2\text{Sn}_2\text{S}_5$ after being contacted by Li metal electrodes. (b) EMF measurement of $\text{Li}_2\text{Sn}_2\text{S}_5$ at 30°C with Li and LiAl as electrodes under high and low pressure. The Nernst voltage for this cell is 0.38 V.⁹

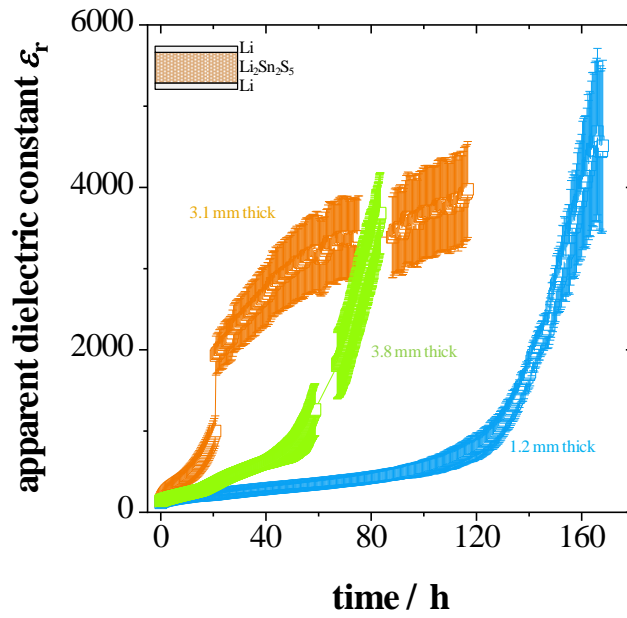


Figure S14: Apparent dielectric constant ϵ_r of anhydrous $\text{Li}_2\text{Sn}_2\text{S}_5$ corresponding to the data shown in Figure S13a.

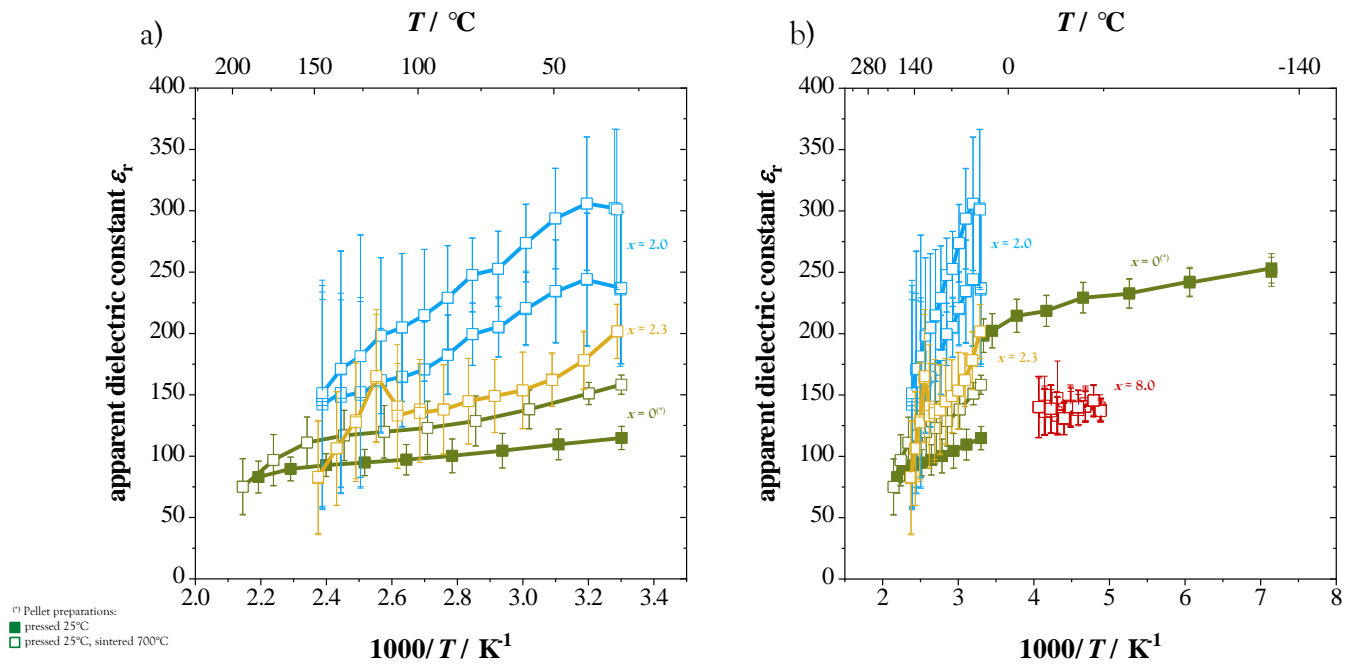


Figure S15: Apparent dielectric constant ϵ_r of $\text{Li}_2\text{Sn}_2\text{S}_5 \cdot x \text{H}_2\text{O}$ over the temperature ranges shown. For $x = 0$, two datasets are shown: pellet pressed at 25°C (closed squares); pellet pressed at 25°C, sintered at 700°C (open squares). For comparison, the dielectric constant of pure liquid water in the kHz range is 80 at 20 °C.¹⁰

Inductively Coupled Plasma Optical Emission Spectroscopy (ICP-OES)

Table S1: ICP-OES results from three samples of anhydrous $\text{Li}_2\text{Sn}_2\text{S}_5$ prepared in separate batches. The last column shows the Li:Sn molar ratio.

$\text{Li}_2\text{Sn}_2\text{S}_5$ ($x = 0$)	wt.% Li	wt% Sn	Li:Sn
Sample 1	3.49	56.82	1.05
Sample 2	3.44	57.71	1.02
Sample 3	3.35	58.43	0.98

Scanning Electron Microscopy (SEM) and Single Crystal Diffraction (SXRD)

Hydrolysis of $\text{Li}_2\text{Sn}_2\text{S}_5$ was ruled out by studying its electron micrographs. The particle morphologies are virtually unchanged by hydration and subsequent dehydration (Figure S16). However, a few lamellar cracks are visible after dehydration, which is to be expected since other layered hydrates such as Li_3InCl_6 also show similar behavior.¹¹ The extent of cracking probably becomes slowly more severe over repeated hydration and dehydration cycles, or if particles are hydrated to a higher x value (cf. Figure 3 in ref. 12). In fact, the covalent bonding in the defective SnS_2 layers of $\text{Li}_2\text{Sn}_2\text{S}_5$ is sufficiently strong that the layers remain intact even after being exfoliated,¹² however, some degree of hydrolysis is observed upon complete immersion in water. The resilience against hydrolysis of lithium tin sulfides is also shown by the compositions Li_2SnS_3 and Li_4SnS_4 (including derivatives), which are stable in humid atmosphere.^{13–19} It must be mentioned that a faint H_2S smell was noticed when $\text{Li}_2\text{Sn}_2\text{S}_5$ powder was exposed to ambient air, indicating only minor hydrolysis owing to the enormous sensitivity of the human nose with respect to H_2S .²⁰ Finally, a TGA measurement performed while switching from argon to pure oxygen observed no change in mass, suggesting that anhydrous $\text{Li}_2\text{Sn}_2\text{S}_5$ is stable towards oxygen as well.

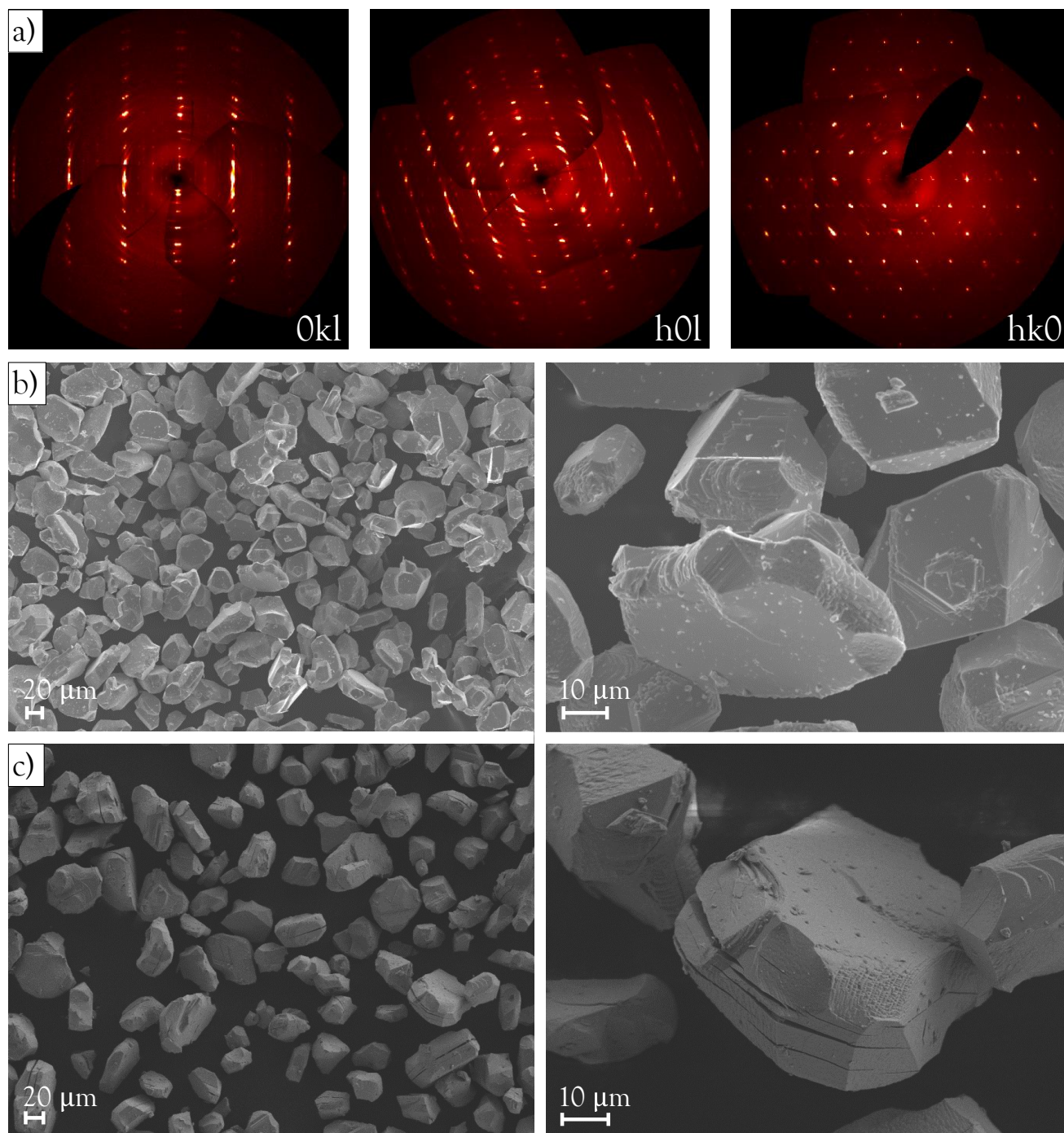


Figure S16: (a) Single crystal diffraction images in reciprocal space of $\text{Li}_2\text{Sn}_2\text{S}_5 \cdot x\text{H}_2\text{O}$ ($x = 0$) of all three net planes. Scanning electron micrographs of $\text{Li}_2\text{Sn}_2\text{S}_5 \cdot x\text{H}_2\text{O}$; (b) $x = 0$; (c) $x \approx 2.7$. In the SEM the sample was exposed to high vacuum ($> 1\ \text{h}$), meaning the images in (c) depict (partially) dehydrated grains.

As shown in the main text, the incorporation of water causes an expansion of the unit cell volume. Naturally, the water will coordinate to Li^+ in the structure, meaning that H_2O molecules will predominantly reside in-between the $(\text{Li}_1, \text{Sn})\text{S}_2$ -sheets. Figure S17 shows a schematic representation how the structure would change upon the incorporation of water molecules, related to the observed behavior from XRD, SEM as well as the change in mechanical properties. The proposed coordination chemistry in $\text{Li}_2\text{Sn}_2\text{S}_5 \cdot x \text{H}_2\text{O}$ between Li^+ and H_2O is in line with findings for the layered mineral vermiculite,^{21–23} in which the water would accommodate between sheets of tetrahedrally coordinated Si/Al cations (units of $\text{Si}_3\text{AlO}_{10}$) and coordinate to an ion exchanged metal cation M (M = Li, Na, Mg, Ca, Ni, Cu).

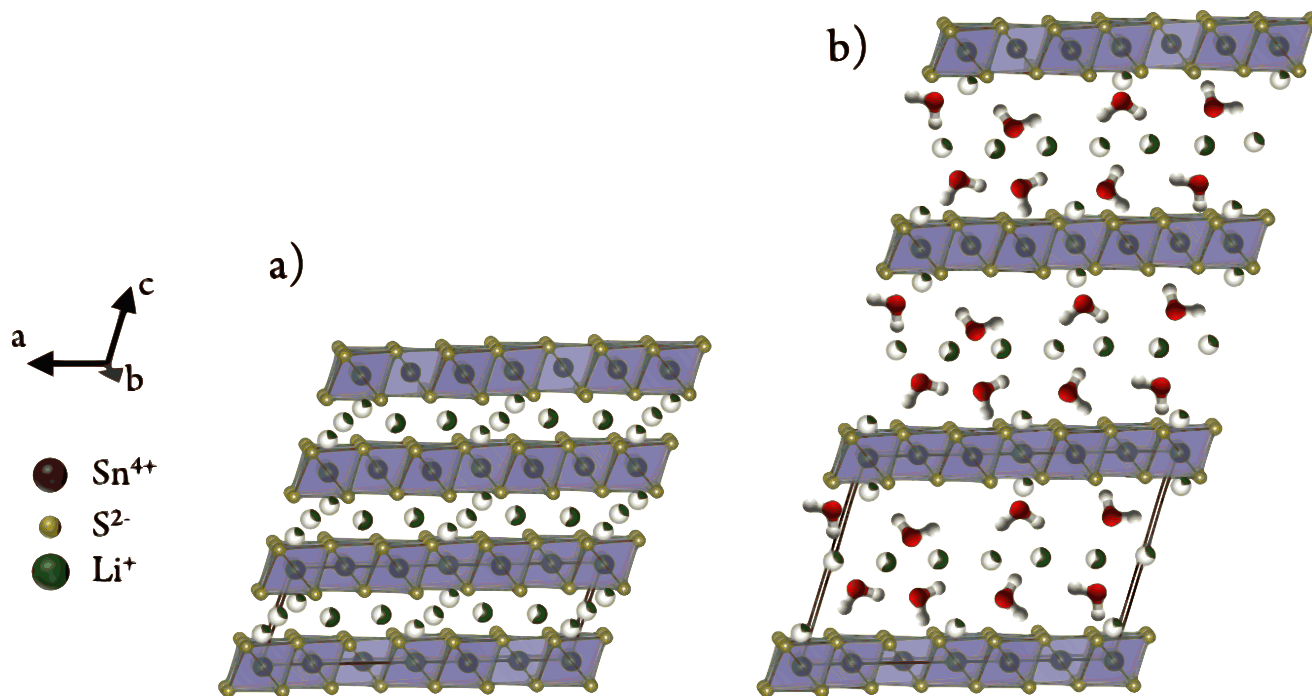


Figure S17: (a) Crystal structure of anhydrous $\text{Li}_2\text{Sn}_2\text{S}_5$; (b) schematic structure of $\text{Li}_2\text{Sn}_2\text{S}_5 \cdot x \text{H}_2\text{O}$.

REFERENCES

- (1) Price, W. S. Pulsed-Field Gradient Nuclear Magnetic Resonance as a Tool for Studying Translational Diffusion: Part I. Basic Theory. *Concepts Magn. Reson.* **1997**, 9 (5), 299–336. [https://doi.org/10.1002/\(sici\)1099-0534\(1997\)9:5<299::aid-cmr2>3.3.co;2-2](https://doi.org/10.1002/(sici)1099-0534(1997)9:5<299::aid-cmr2>3.3.co;2-2).
- (2) Kimmelerle, F.; Majer, G.; Kaess, U.; Maeland, A. J.; Conradi, M. S.; McDowell, A. F. NMR Studies of Hydrogen Diffusion in ZrBe₂H_{1.4}. *J. Alloys Compd.* **1998**, 264 (1–2), 63–70. [https://doi.org/10.1016/S0925-8388\(97\)00273-9](https://doi.org/10.1016/S0925-8388(97)00273-9).
- (3) Bruker Suite Version 2019/1, Bruker AXS Inc., Madison, WI, USA. Bruker AXS Inc.: Madison, WI, USA 2019.
- (4) Maier, J. *Physical Chemistry of Ionic Materials*; John Wiley & Sons, Ltd, 2004.
- (5) Holzmann, T.; Schoop, L. M.; Ali, M. N.; Moudrakovski, I.; Gregori, G.; Maier, J.; Cava, R. J.; Lotsch, B. V. Li_{0.6}[Li_{0.2}Sn_{0.8}S₂] – a Layered Lithium Superionic Conductor. *Energy Environ. Sci.* **2016**, 9 (8), 2578–2585. <https://doi.org/10.1039/C6EE00633G>.
- (6) L. Sudmeier, J.; E. Anderson, S.; S. Frye, J. Calculation of Nuclear Spin Relaxation Times. *Concepts Magn. Reson.* **1990**, 2 (4), 197–212. <https://doi.org/10.1002/cmr.1820020403>.
- (7) Kuhn, A.; Narayanan, S.; Spencer, L.; Goward, G.; Thangadurai, V.; Wilkening, M. Li Self-Diffusion in Garnet-Type Li₇La₃Zr₂O₁₂ as Probed Directly by Diffusion-Induced ⁷Li Spin-Lattice Relaxation NMR Spectroscopy. *Phys. Rev. B - Condens. Matter Mater. Phys.* **2011**, 83 (9), 1–11. <https://doi.org/10.1103/PhysRevB.83.094302>.
- (8) Waugh, J.; Fedin, E. Determination of Hindered-Rotation Barriers in Solids. *Sov. Physics-Solid State* **1963**, 4 (8), 1633–1636.
- (9) Wen, C. J.; Boukamp, B. A.; Huggins, R. A.; Weppner, W. Thermodynamic and Mass Transport Properties of “LiAl.” *J. Electrochem. Soc.* **1979**, 126 (12), 2258. <https://doi.org/10.1149/1.2128939>.
- (10) Sears, F. W.; Zemansky, M. W.; Young, H. D. University Physics. Addison-Wesley Pub. Co.: Reading, Mass. 1982.
- (11) Sacci, R. L.; Bennett, T. H.; Drews, A. R.; Anandan, V.; Kirkham, M. J.; Daemen, L. L.; Nanda, J. Phase Evolution during Lithium-Indium Halide Superionic Conductor Dehydration. *J. Mater. Chem. A* **2021**, 9 (2), 990–996. <https://doi.org/10.1039/d0ta10012a>.
- (12) Kuhn, A.; Holzmann, T.; Nuss, J.; Lotsch, B. V. A Facile Wet Chemistry Approach towards Unilamellar Tin Sulfide Nanosheets from Li₄Sn_{1-x}S₂ Solid Solutions. *J. Mater. Chem. A* **2014**, 2 (17), 6100–6106. <https://doi.org/10.1039/C3TA14190J>.
- (13) Kaib, T.; Haddadpour, S.; Kapitein, M.; Bron, P.; Schröder, C.; Eckert, H.; Roling, B.; Dehnen, S. New Lithium Chalcogenidotetrelates, LiChT: Synthesis and Characterization of the Li⁺-Conducting Tetralithium Ortho-Sulfidostannate Li₄SnS₄. *Chem. Mater.* **2012**, 24 (11), 2211–2219. <https://doi.org/10.1021/cm3011315>.
- (14) MacNeil, J. H.; Massi, D. M.; Zhang, J.-H.; Rosmus, K. A.; Brunetta, C. D.; Gentile, T. A.; Aitken, J. A. Synthesis, Structure, Physicochemical Characterization and Electronic Structure of Thio-Lithium Super Ionic Conductors, Li₄GeS₄ and Li₄SnS₄. *J. Alloys Compd.* **2014**, 586, 736–744. <https://doi.org/10.1016/j.jallcom.2013.10.011>.
- (15) Sahu, G.; Lin, Z.; Li, J.; Liu, Z.; Dudney, N.; Liang, C. Air-Stable, High-Conduction Solid Electrolytes of Arsenic-Substituted Li₄SnS₄. *Energy Environ. Sci.* **2014**, 7 (3), 1053–1058. <https://doi.org/10.1039/c3ee43357a>.
- (16) Brant, J. A.; Massi, D. M.; Holzwarth, N. A. W.; Macneil, J. H.; Douvalis, A. P.; Bakas, T.; Martin, S. W.; Gross, M. D.; Aitken, J. A. Fast Lithium Ion Conduction in Li₂SnS₃: Synthesis, Physicochemical Characterization, and Electronic Structure. *Chem. Mater.* **2015**, 27 (1), 189–196. <https://doi.org/10.1021/cm5037524>.
- (17) Park, K. H.; Oh, D. Y.; Choi, Y. E.; Nam, Y. J.; Han, L.; Kim, J. Y.; Xin, H.; Lin, F.; Oh, S. M.; Jung, Y. S. Solution-Processable Glass LiI-Li₄SnS₄ Superionic Conductors for All-Solid-State Li-Ion Batteries. *Adv. Mater.* **2016**, 28 (9), 1874–1883. <https://doi.org/10.1002/adma.201505008>.
- (18) Choi, Y. E.; Park, K. H.; Kim, D. H.; Oh, D. Y.; Kwak, H. R.; Lee, Y. G.; Jung, Y. S. Coatable Li₄SnS₄ Solid Electrolytes Prepared from Aqueous Solutions for All-Solid-State Lithium-Ion Batteries. *ChemSusChem* **2017**, 10 (12), 2605–2611. <https://doi.org/10.1002/cssc.201700409>.
- (19) Kwak, H.; Park, K. H.; Han, D.; Nam, K. W.; Kim, H.; Jung, Y. S. Li⁺ Conduction in Air-Stable Sb-Substituted Li₄SnS₄ for All-Solid-State Li-Ion Batteries. *J. Power Sources* **2020**, 446, 227338. <https://doi.org/10.1016/j.jpowsour.2019.227338>.
- (20) Leonardos, G.; Kendall, D.; Barnard, N. Odor Threshold Determinations of 53 Odorant Chemicals. *J. Air Pollut. Control Assoc.* **1969**, 19 (2), 91–95. <https://doi.org/10.1080/00022470.1969.10466465>.
- (21) Whittingham, M. S. Sodium Ion Conduction in Single Crystal Vermiculite. *Solid State Ionics* **1987**, 25, 295–300. [https://doi.org/https://doi.org/10.1016/0167-2738\(87\)90193-7](https://doi.org/https://doi.org/10.1016/0167-2738(87)90193-7).
- (22) Stanley Whittingham, M. Transport Properties of the Mineral Vermiculite. *Solid State Ionics* **1989**, 32/33, 344–349. [https://doi.org/10.1016/0167-2738\(89\)90239-7](https://doi.org/10.1016/0167-2738(89)90239-7).
- (23) Whittingham, M. S. Hydrogen Motion in Oxides: From Insulators to Bronzes. *Solid State Ionics* **2004**, 168 (3–4), 255–263. <https://doi.org/10.1016/j.ssi.2003.08.056>.